Edge Loss of High-Harmonic Fast-Wave Heating Power in NSTX: a Cylindrical Model

R. J. Perkins and J. C. Hosea and N. Bertelli and G. Taylor and J. R. Wilson

Princeton Plasma Physics Laboratory, Princeton, NJ 08540

(Dated: January 17, 2017)

Abstract

Efficient high harmonic fast-wave (HHFW) heating on the National Spherical Torux eXperiment Upgrade (NSTX-U) would facilitate experiments in turbulence, transport, fast-ion studies, and more. However, previous HHFW operation on NSTX exhibited a large loss of fast-wave power to the divertor along scrape-off-layer field lines for edge densities above the fast-wave cutoff. It was postulated that the wave amplitude is enhanced in the scrape-off layer due to cavity-like modes, and that these enhanced fields drive sheath losses through RF rectification. As part of ongoing work to confirm this hypothesis, we have developed a cylindrical cold-plasma model to identify and understand scenarios where a substantial fraction of wave power is confined to the plasma periphery. We previously identified a peculiar class of modes, named annulus resonances, that conduct approximately half of their wave power in the periphery and can also account for a significant fraction of the total wave power. Here, we study the influence of annulus resonances on wave-field reconstructions and find instances where the annulus resonant modes dominate the spectrum and trap over half of the total wave power in the edge. The work is part of an ongoing effort to determine the mechanism underlying these scrape-off layer losses on NSTX, identify optimal conditions for operation on NSTX-U, and predict whether similar losses occur for the ion-cyclotron minority heating scheme both for current experiments and future devices such as ITER.

I. INTRODUCTION

High-harmonic fast-wave (HHFW) heating is a promising heating scheme for the National Spherical Torus eXperiment Upgrade (NSTX-U). HHFW compliments neutral beam injection by heating discharges without particle or momentum input. Efficient HHFW heating would enable experiments in transport studies [1], low-rotation scenarios, and fast-particle modes [2]. Furthermore, as the plasma-facing tiles of NSTX-U transitions from graphite to high-Z metal wall in the coming years, HHFW may play a crucial role in impurity expulsion via central RF heating, as demonstrated in other devices [3, 4].

Unfortunately, efficient fast-wave heating was difficult to achieve in certain NSTX scenarios. Poor heating efficiency was observed for lower phasing and lower toroidal field [5, 6] but improved with the lower scrape-off-layer (SOL) density provided by lithium wall conditioning, provided that the machine was not vented to produce lithium compounds [7]. The lower heating efficiency is likely caused by a direct loss of wave power to the SOL, as evidenced by the bright spirals that form in the upper and lower diveror [8] along field lines passing in front of the antenna [9]. The heat flux under the spiral is about 2 MW/m^2 for an applied HHFW power of 1.8 MW. The losses are now though to be caused by significant fast-wave propagation in the SOL when the righthand cutoff layer, defined by $n_\parallel^2 = R$, with $n_\parallel$ the parallel refractive index and R the cold-plasma dielectric component from Stix notation [10], was positioned close to the antenna [6]. Subsequent conversion of the wave power to a heat flux would believed to be caused by RF rectification [11]. Full-wave simulations of NSTX using the full-wave code AORSA [12] with the solution domain extended to include the SOL [13] show that the wave amplitude in the SOL growing to large values when the SOL density exceeds the cutoff density in front of the antenna [14]. We believe that NSTX-U discharges can be taylored to achieve efficient HHFW heating, asthere have been several instances of successful HHFW operation, including record-high T_e obtained from HHFW-only discharges[15], and plasmas that were 70% non-inductive [16].

We have developed a cylindrical cold-plasma model to identify scenarios where significant wave power is trapped in the edge plasma. The model lacks many details included in full-wave codes but provides a simplified framework to study wave-propagation across a steep edge density gradient. We previously identified a peculiar class of modes, called annulus resonances, that have enhanced loading resistance and propagate significant power

in the edge [17]. They are thus strong candidates to explain the edge losses on NSTX, and the present paper the annulus-resonances influence on the reconstructed wave fields. This paper is structured as follows. Section II describes the model and the parameters chosen to represent NSTX discharges. Section III explores properties of the annulus resonance with respect to m, the azimuthal mode number. In Sec. IV, the impact of the annulus resonance on the wave-field reconstruction is evaluated for a scan of the edge density. We find instances where the annulus resonant modes dominate the spectrum and over half the wave power is trapped in the edge. We find other instances where the annulus resonant modes are less dominant and over 80% of the wave power propagates in the core. That being said, the scaling of edge power percentage with edge density obtained in the model do not always match experimental trends, and Sec. V discusses the potential influence of field pitch in this discrepancy.

II. DESCRIPTION OF THE MODEL AND THE CHOICE OF PARAMETERS

The model geometry, illustrated in Fig. 1, consists of three radial regions: a core plasma, a lower-density annulus, and an outer vacuum region. The annulus region represents the SOL, and the vacuum region represents the extremely low density region behind the limiter and inside the antenna box. The core extends to radius r_c with constant density n_c. The annulus extends from $r = r_c$ to r_a with constant density n_a. The vacuum region extends from $r = r_a$ up to a conducting wall of radius r_w. The two-step density profile surrounded by vacuum is a coarse approximation of the actual density but is partially justified on the basis that SOL density profiles are relatively steep near the separatrix but become nearly flat in the mid- to far-SOL [18, 19]. The perpendicular wavelength of the fast wave in the SOL is at smallest around 7 cm and is typically much larger; therefore, approximating a gradient of scale length 1 - 2 cm [20] is not obscene. A uniform axial magnetic field is used throughout. The use of a uniform magnetic field is partially justified since the focus of our study in on the SOL, over which the magnitude and direction of the magnetic field does not change appreciably, at least not as much as the density. The larger error comes in neglecting the poloidal field, which is substantial on NSTX. Field angles $\tan^{-1}(B_{\rm pol}/B_{\rm tor})$ up to 40° have been measured during HHFW experiments. The potential impact of this sizable tilt is discussed in Sec. V, but we note that large RF field amplitudes were observed in simulations

using only a toroidal field [21]. The antenna is modelled as current straps carrying current in the θ direction at $r = r_s$ with a Faraday screen at $r = r_F$.

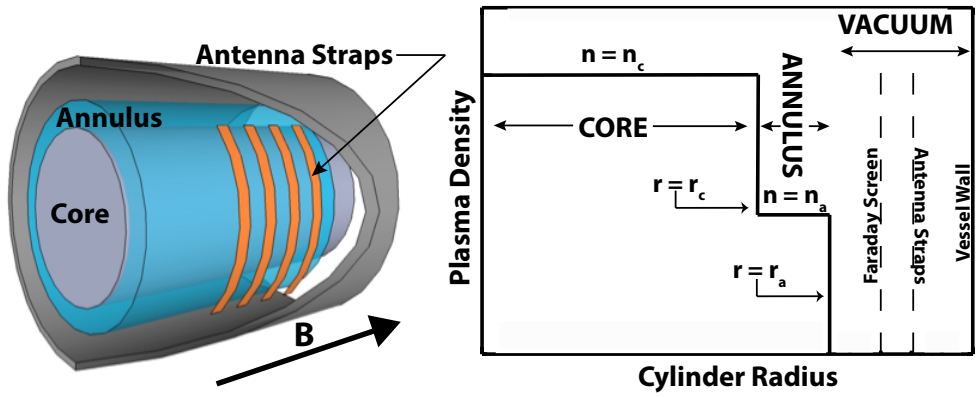

FIG. 1: (a) Cartoon of the model showing the two-step density profile and orientiation of the antenna straps. (b) Radial density profile (not to scale) along with radial position of antenna.

We chose values for the model parameters that resemble as much as possible NSTX discharges. For radii, we use a core radius of $r_c = 0.88$ m, an annulus outer radius of $r_a = 0.915$ m, a Faraday-screen radius of $r_F = 0.9315$ m, and a wall radius of $r_w = 0.9715$ m. The model core radius is chosen to keep the plasma cross-section area roughly the same as shot 120740, yielding an effective circular radius of 0.88 m. The annulus width $r_a - r_c$ chosen to be 3.5 cm based on average values of the experimental "outer gap" as determined from equilibrium magnetics for the L-mode discharges studied in Ref. [6]. The distance from the edge of the annulus to the Faraday screen is fixed at 1.65 cm, the distance between the outer boron nitride limiter and the Faraday screen at the midplane. The distances from the Faraday screen to the antenna strap is likewise fixed at 2 cm, and from the antenna to the vacuum wall at 2cm. $n_c = 5 \times 10^{19}$ m^{-3}, $f = 30$ MHz, $B = 0.32$ T (approximate field at the edge for a 0.55 T on-axis field).

A "mode" refers to a global solution which satisfies the wave equation in each region and which is matched at interfaces. Modes assume the form $\tilde{E}_z(r, m, k_\parallel) = \tilde{E}_z(r) \exp(im\theta + ik_\parallel z - i\omega t)$, based on Fourier analysis in the axial and azimuthal directions. With $k_\parallel$ given, $k_\perp$ is fixed in each region by the plasma regions by the cold-plasma dispersion: we use the notation $k_{\perp,c}^{\text{fast}}$ and $k_{\perp,c}^{\text{slow}}$ for the fast/slow wave $k_\perp$ in the core and corresponding notation $k_{\perp,a}^{\text{fast}}$ and $k_{\perp,a}^{\text{slow}}$ in the annulus. The slow-wave and vacuum $k_\perp$ are always cutoff. Radial RF field profiles are found by the method detailed in Ref. [22]. Each region admits four

independent solutions. In plasma, there are two fast-wave solutions and two (cutoff) slow-wave solutions; in vacuum there are exponentially decaying and growing E_z (transverse magnetic) and H_z (transverse electric) modes. By specifying the boundary conditions are each interface, a system of equations is developed, whose simultaneous solution only exists when a determinant, denoted by the function $F(k_\parallel)$ vanishes, as described in Ref. [17]. As might be anticipated for oscillation in a bounded system, the roots of $F(k_\parallel)$ are such that an integral number of half wavelengths occur in the radial profile of E_θ. Thus, we can label modes with two numbers, (m, n), with m the azimuthal wavenumber and n the radial mode number. Because the fast-wave dispersion gives $k_\perp$ as a decreasing function of $k_\parallel$, lower n corresponds to larger $k_\parallel$.

The total fields are found by inverse Fourier transform:

$$E_\theta = \sum_m \int \tilde{E}_\theta(r, m, k_\parallel) \tilde{J}_{\rm ant}(m, k_\parallel) e^{im\theta + ik_\parallel z} dk_\parallel, \tag{1}$$

The expression for $\tilde{E}_\theta$ contains $F(k_\parallel)$ in the denominator, so that the integral reduces to a sum of residues, one for each mode. In Eq. (1), $\tilde{J}_{\rm ant}(m, k_\parallel)$ is the antenna spectral current density and $\tilde{E}_\theta$ the azimuthal electric field per unit antenna spectral current density. The amplitude of each mode is thus given by two factors: (i) the amplitude of $\tilde{J}_{\rm ant}(m, k_\parallel)$ at the $k_\parallel$ and m of the mode, and (ii) the size of the residue, which is proportional to $(dF(k_\parallel)/dk_\parallel)^{-1}$. As described in Ref. [17], the large amplitude of an annulus resonance is due to a near vanishing of $dF(k_\parallel)/dk_\parallel$ independent of the particulars of the antenna configuration. Indeed, this paper describes the relative influence between antenna spectral weighting and "bare" mode amplitude in the relative strength of annulus resonances.

The antenna strap current distribution is modelled as twelve infinitely thin filaments. The Fourier spectrum in the axial direction is therefore a sum of twelve plane waves. Given that the height of the antenna straps is 68.9 cm, and using the effective plasma radius above, we approximate the antenna angular span as 0.724 radians in the model. We assume a uniform current distribution in the azimuthal (poloidal) direction due to the long vacuum wavelength compared to the strap length. Given a phase difference of ϕ between straps, a strap spacing of d and the current of each I_0 and an angular span of α,

$$\begin{aligned} J_{\rm ant}(r, \theta, z) = I_0 \delta(r - r_a) \left[\Theta(\theta + \alpha/2) - \Theta(\theta - \alpha/2)\right] \times \\ \sum_{i=0}^{12} \delta(z + (11 - 2i)d/2) e^{-i\phi(11-i)/2} \end{aligned} \tag{2}$$

where Θ is a Heaviside step function. J_{ant} can be decomposed into a Fourier series in the azimuthal direction and a Fourier transform in the axial direction

$$\tilde{J}_{\text{ant}}(r, m, k_{\|}) = I_0 \delta(r - r_a) \tilde{J}_\theta(m) \tilde{J}_{\|}(k_{\|}) \tag{3}$$

$$\tilde{J}_\theta(m) = \frac{\sin(m\alpha/2)}{m\pi} \tag{4}$$

$$\tilde{J}_{\|}(k_{\|}) = \sum_{i=0}^{12} e^{ik_{\|}(11-2i)d/2} e^{-i\phi(11-i)/2} \tag{5}$$

We note that $\tilde{J}_\theta$ scales as $1/m$ and is nearly zero whenever $m\alpha/2$ is an integer multiple of π. This clearly favors low m modes. On the other hand, $\tilde{J}_{\|}$ is peaked around $k_{\|} = \phi/d$. For NSTX, $d = 21.5$ cm, and typically phasings are $\pi/6$, $\pi/2$ and $5\pi/6$. This model clearly ignores (i) the finite width of the antenna straps, (ii) the radial feeds, (iii) effects of sidewalls [23], and (iv) the change in current along the length of the straps.

In this paper, the term "mode amplitude" refers to the amount of wave power a mode conducts axially along the cylinder. We denote the amplitude of the (m, n) mode as $P_{m,n}$ but will also express this as a loading resistance $R_{m,n}$ defined by $R_{m,n} I_0^2/2 = P_{m,n}$, with I_0 defined in Eq. (2). $P_{m,n}$ can be calculated as the power output of the antenna, also refered to as the induced EMF method [24].

$$P_{m,n} = \int \left\langle \tilde{\mathbf{E}}(r, m, k_{\|}) \cdot \tilde{\mathbf{J}}_{\text{ant}}(m, k_{\|})^* \right\rangle dV, \tag{6}$$

where $< \ldots >$ denotes time-averaging of complex quantities. Equivalently, $P_{m,n}$ can be computed by integrating the axial Poynting flux over the cross-section of the cylinder

$$P_{m,n} = \int_{r=0}^{r=r_w} \int_{\theta=0}^{\theta=2\pi} \hat{z} \cdot \left\langle \mathbf{E}(r, m, k_{\|}) \times \mathbf{H}(r, m, k_{\|})^* \right\rangle r dr d\theta, \tag{7}$$

Equation 7 gives the same result regardless of the z position used to evaluate the integral, and both Eq. (6) and (7) yield the same result, as expected for a system without dissipation.

We emphasize that this cylindrical model is motivated by the need to qualitatively understanding and is not intended for precise calculations of loading resistances. The model is cylindrical, so toroidal effects are clearly excluded. The model does not include any of the surrounding the strap and Faraday screen; substantial research has been done to study the effects of such components, especially when misaligned with the magnetic field and their possible excitation of an electric field component parallel to the background magnetic field. Finite-temperature and non-linear effects are omitted, including conversion to ion Bernstein

waves, parametric decay instability, and RF rectification. Indeed, no form of dissipation is included; wave energy coupled from the antenna propagates out the ends of the cylinder without absorption. The mechanism converting HHFW power in the SOL to a divertor heat flux is not yet identified, but dissipation by far-field RF sheaths is a leading candidate [11]. Core absorption is the usual Landau damping and transit-time magnetic pumping. We presume that the high edge field amplitude of the annulus resonance will drive a high rate of edge absorption relative to core absorption once the proper SOL damping mechanism is identified and included, but this remains a crucial future step to verify. We also observe that this present model treats the tokamak as a plasma-filled waveguide, whereas the AORSA simulations including the SOL resemble more a plasma-filled cavity. We emphasize again that the cylindrical model allows for relatively rapid computation time and faster exploration of parameter space as well as the ability to resolve individual modes and separate the contribution between fast and slow waves.

III. PROPERTIES OF ANNULUS RESONANCES OVER SEVERAL AZIMUTHAL MODE NUMBERS

The annulus resonance condition is that a half-wavelength structure in E_θ fits into in the combined annulus/vacuum regions. The modes that most nearly satisfy this condition have a greatly enhanced loading resistance and propagate over half of their wave power in the edge. What we call "annulus resonant modes" are the mode, for each m, the most closely satisfies this condition and consequently has the largest loading resistance. Indeed, when the bare loading resistances for all modes of a single m are plotted against $k_\parallel$, the annulus resonances, if present, appears as a peak in an otherwise monotonically decreasing curve, as shown in Fig. 2. "Bare" loading resistance means omitting the factor of $\tilde{J}_{ant}(m, k_\parallel)$ in Eq. (1); alternatively, it is the loading resistance calculated using a point-source antenna $J_{\rm ant}(\theta, z) = I_0\delta(z)\delta(\theta)$, which gives a uniform power spectrum. For the typical SOL parameters modelled here, one generally finds at most one annulus resonance per m. It is possible at there is no annulus resonance present, as shown in Fig. 2.

This section will focus on the behavior of these modes for different m. As mentioned, there is typically at most one annulus resonance per m, but the $k_\parallel$ of the resonance increases with m. This is demonstrated in Fig. 3.a, where the bare loading resistance is plotted against

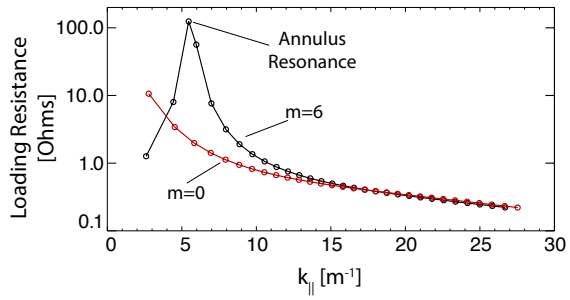

FIG. 2: Bare loading resistance for $m = 6$ (black) and $m = 0$ modes (red) for an annulus density of 1.5×10^{18} m^{-3}, showing typical loading-resitance curves with and without an annulus resonance.

$k_\parallel$ for select azimuthal mode numbers m. There is one annulus resonance for every m, and the $k_\parallel$-value of these peaks increases with increasing m. For low enough m (in this case, $m \leq 0$), this peak begins to disappear into the vacuum cutoff $k_\parallel = \omega/c$. In Fig. 3.b, the $k_\parallel$ value of the largest mode for each m is plotted against m; there appears to be a functional relationship. Figure 3.c is similar to Figure 3.b except the vertical axis is $k_{\perp,c}^{\text{fast}}$, the fast wave $k_\perp$ in the core. This last plot appears piecewise linear with "breaks," consecutive modes that have similar $k_{\perp,c}^{\text{fast}}$.

Figure 3.b is important to understand. The "trajectory" of the annulus resonance condition through $k_\parallel - m$ space determines whether or not these modes will intercept the peaks on the antenna spectrum. It is also important to understand how parameters such as magnetic field and annulus density effect this "trajectory."

A. Radial Mode Number n

In Sec. II, we introduced the radial mode number n as the number of zeros in the radial profile of E_θ. We now derive approximate analytic expressions for the $k_\parallel$-spacing between modes of consecutive n and fixed m and also for consecutive m and fixed n. To start, most of the zeros in the radial E_θ profile occur in the core because the core is the largest region and also because $k_\perp^{\text{fast}}$ is realtively large there due to the higher density. The core fast wave fields are linear combinations the Bessel functions $J_m(k_{\perp,c}^{\text{fast}}(m,n)r)$ and $J_{m+1}(k_{\perp,c}^{\text{fast}}(m,n)r)$ and can be approximated by their asymptotic forms:

$$J_m(k_{\perp,c}^{\text{fast}}(m,n)r) \approx \sin\left(k_{\perp,c}^{\text{fast}}(m,n)r - m\frac{\pi}{2} - \frac{\pi}{4}\right). \tag{8}$$

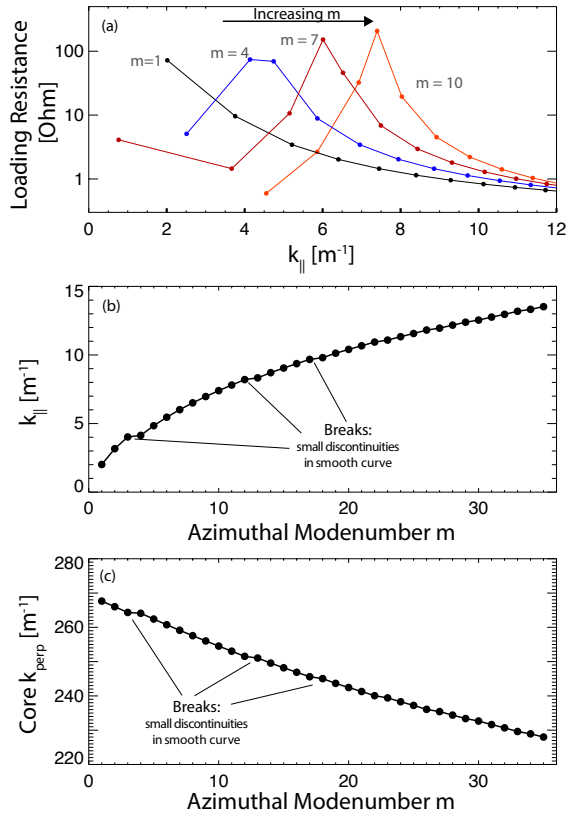

FIG. 3: (a) Loading resistance versus $k_{\|}$ for $m = 1$ (black), $m = 4$ (blue), $m = 7$ (red), and $m = 10$ (orange) modes. The $k_{\|}$ of the annulus resonances increases with increasing m. (b) The $k_{\|}$ value of the largest mode for each m. (c) As in b) but with $k_{\perp,c}^{\text{fast}}$ as the abscissa. $n_a = 1.5 \times 10^{18}$ m^{-3}.

If we define $\phi_{m,n}$ to be the phase argument in Eq. (8),

$$\phi_{m,n} \approx k_{\perp,c}^{\text{fast}}(m,n)r - m\frac{\pi}{2} - \frac{\pi}{4}, \tag{9}$$

then $\phi_{m,n}$ is an approximation to the fast wave phase at the core-annulus boundary. We then conjecture that $\phi_{m,n+1}$ is greater than $\phi_{m,n}$ by a value of π to produce an extra zero in the radial profile of E_θ in the core. Then

$$k_{\perp,c}^{\text{fast}}(m,n+1) = k_{\perp,c}^{\text{fast}}(m,n) + \frac{\pi}{r_c}, \tag{10}$$

where the notation $k_{\perp,c}^{\text{fast}}(m,n)$ denotes the value of $k_{\perp,c}^{\text{fast}}$ for mode of azimuthal number m and radial mode number n. Similarly, we conjecture that $\phi_{m+1,n} \approx \phi m, n$, since both modes

have the same number of zeros. This conjecture leads to

$$k_{\perp}^{\text{fast}}(m, n+1) = k_{\perp}^{\text{fast}}(m, n) + \frac{\pi}{2r_c}. \tag{11}$$

Increasing $k_{\perp,c}^{\text{fast}}$ means decreasing $k_{\parallel}$. In either case, the changes in $k_{\parallel}$ is found by solving the fast-wave dispersion:

$$n_{\perp}^2 = \frac{(R - n_{\parallel}^2)(L - n_{\parallel}^2)}{S - n_{\parallel}^2}. \tag{12}$$

with n the refractive index $n = ck/\omega$.

Both conjectures assume that any change in radial phase between modes occurs primarily in the core and that the change in the combined annulus-vacuum region is small. The impact of the phase change will be shown below. We note that the term "radial phase" is a fuzzy concept for the edge; the wave fields are radially cutoff in the vacuum and sometimes also in the annulus. Moreover, discontinuous jumps in phase occur at sharp interfaces such as the ones used in this model.

We now compare the predictions made by Eqs. (10) and (11) to the modes computed by the model. Figure 4a plots the asymptotic core fast-wave phase for $m = 14$ modes, $\phi_{14,n}$, as a function of n. The resulting plot is remarkably linear with slope π as predicted above. At $n = 65$, there is a joggle in the linear trend. The $n = 65$ $m = 14$ mode is an annulus resonance and will be discussed below. Figure 4b plots $\phi_{m,65}$ versus m from $m = 1$ to $m = 18$; for larger m, the annulus resonance disappears into the vacuum cutoff $k_{\parallel} = \omega/c$. For $m < 14$, the curve is very flat; the percent change in $\phi_{m,65}$ from $m = 1$ to $m = 13$ is 0.37%. This insensitivity of $\phi_{m,n}$ to n is consistent with Eq. (11). The deviation from flatness is likely due to the much smaller variation in phase across the annulus/vacuum regions. Like Fig. 4b, there is an abrupt change in phase at the annulus resonance $m = 14$ $n = 65$. Annulus resonances have a unique fast-wave phase at the core-annulus boundary that is roughly $\pi/2$ radians out of phase with other modes [17], which explains the abrupt phase change in both figures.

If the plot in Fig. 4 is extended to $m < 1$, the phase $\phi_{m,65}$ would increase linearly. This, however, is an artifact of the asymptotic phase $\phi_{m,n}$. Because $J_{-m}(x) = (-1)^m J_m(x)$ for integral m, the negative m modes behave similarly to their positive counterparts.

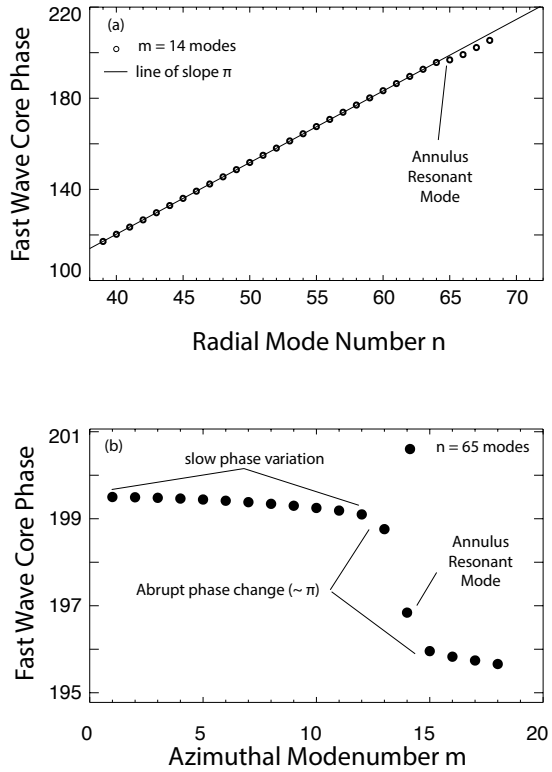

FIG. 4: (a) Core phase $\phi_{14,n}$ for the $m = 14$ mode as a function of n. A straight line with slope π is drawn for reference. (b) Core phase $\phi_{m,65}$ for the $n = 65$ radial mode as a function of m; note the change in vertical scale. For both figures, $n_a = 1.5 \times 10^{18}$ m^{-3}.

B. Mode Families

This section explains the piece-wise linear dependence of $k_{\perp,c}^{\text{fast}}$ of annulus resonant modes versus m seen in Fig. 3. Figure 5a is a scatter plot of loading resistance versus $k_{\|}$ for all modes from $m = 0$ to $m = 40$. Figure 5a is similar to Fig. 3 but has a logarithmic vertical scale, more azimuthal mode numbers, and no coloring to distinguish the m-values of modes. This annulus resonant modes lie at the top of this figure. Certain sets of modes appear to lie on smooth curves in Fig. 5; these curves rise to a crest and then decrease with increasing $k_{\|}$, with the envelope of these curves being the set of annulus resonant modes. These smooth curves are not defined by modes of the same m value; Fig. 5b demonstrates this by repeating the scatter plot with modes of the same m joined by colored curves. Instead, the smooth curves are defined by all modes whose sum $m + n$ is equal; we refer to such sets as families.

In Fig. 5c, modes with equal $m + n$ joined by colored to differentiate families. For the simulation used for Fig. 5, the $m + n = 78$ family is the dominant family for $k_{\|}$ between 4 and 8 m^{-1} and contains the annulus resonances for $m = 4$ to $m = 12$. Above $k_{\|} \approx 8$ m^{-1}, the loading resistance of the $m + n = 78$ family declines as the loading of the $m + n = 79$ family increases. The annulus resonances between $k_{\|} = 8$ m^{-1} and $k_{\|} = 9.7$ m^{-1} belong to the $m + n = 79$ family. The transition between families is emphasized by the $m = 4$ modes, colored blue in Fig. 5b. The annulus resonance peak in loading resistance for these modes is broader than usual (compare the $m = 4$ modes to the $m = 7$ and $m = 10$ modes in the same figure, or to Fig. 2). This peak consists of two closely spaced and nearly equal modes, each coming from a different family as the annulus resonance condition transitions from the $m + n = 77$ curve to the $m + n = 78$ curve.

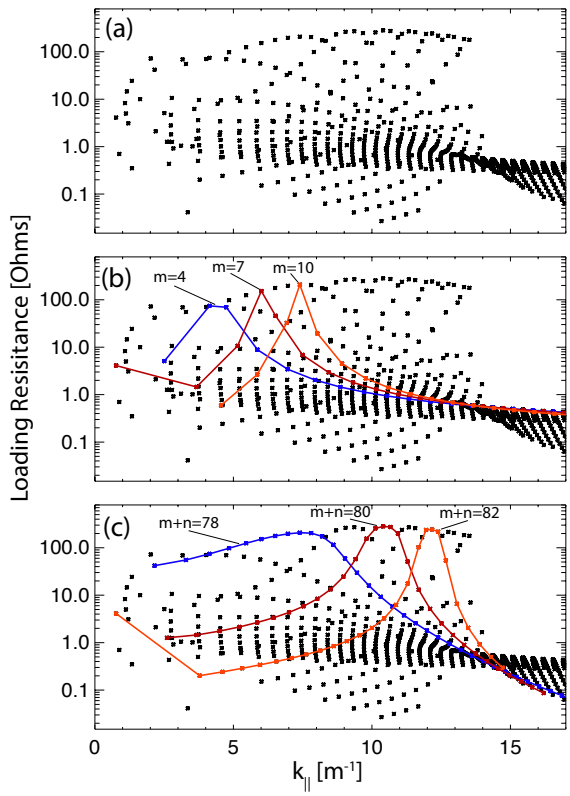

FIG. 5: (a) Scatter plot of loading resistance versus $k_{\|}$ for all modes. (b) Same as (a) with $m = 4$ (blue), $m = 7$ (red), and $m = 10$ (orange) modes joined by colored lines. (c) Same as (a) with $m + n = 78$ (blue), $m + n = 80$ (red), and $m + n = 82$ (orange) modes joined by colored lines.

Within a family, the outermost half wavelength varies relatively slowly across modes. Figure 6 shows this variation for two cases: for fixed m and varying n, and for $m + n$

fixed. In the lefthand column, m is fixed at 6, and n decreases by one from 73 (Fig. 6a) to 72 (Fig. 6b) to 71 (Fig. 6c). The outermost half wavelength grows and sweeps across the annulus-core boundary. The $n = 72$ mode most nearly satisfies the annulus resonance condition and correspondingly has the largest amplitude. In the righthand column of Fig. 6, n decreases by one and m increeases by one, going from $m = 5$ and $n = 73$ (Fig. 6d) to $m = 6$ and $n = 72$ (Fig. 6e) to $m = 7$ and $n = 71$ (Fig. 6f). The outermost half wavelength now varies almost imperceptibly and closely satisfies the annulus resonance condition. As one continues to increment m and decrement n keeping $m + n$ constant, the outermost half wavelength eventually growths larger than the edge width, losing the annulus resonance condition and leading to the fall off in mode amplitude. However, as the $m + n = 78$ family falls off, the $m + n = 79$ family begins to satisfy the annulus resonance condition more closely. It is currently not clear why holding $m + n$ constant slows the variation in the outermost half wavelength.

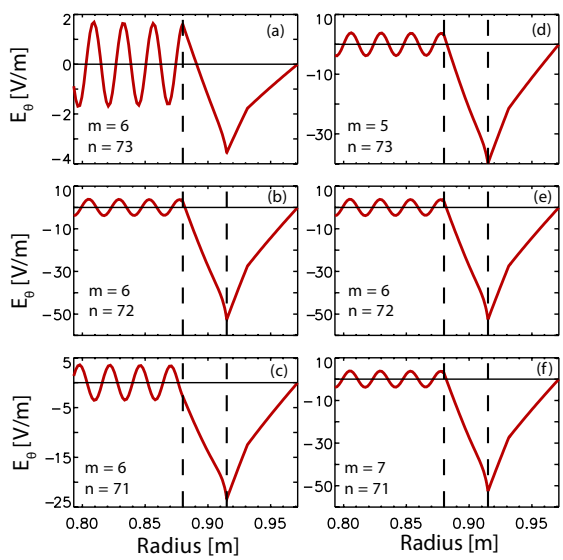

FIG. 6: Radial profiles of E_θ for various modes. In the left column, m is fixed at $m = 6$ and n decreases by one moving down. In the right column, m increases by one while n decreases by one moving down.

The dependence of $k_{\perp,c}^{\text{fast}}$ and $k_\parallel$ of the annulus resonance on m, Figs. 3c and 3b respectively, can be found by applying Eq. 11 within a family, so that $m + n =$ constant.

$$k_{\perp,c}^{\text{fast}}(m+1, n-1)r_c = k_{\perp,c}^{\text{fast}}(m, n)r_c - \frac{\pi}{2}. \tag{13}$$

from which the $k_{\|}$-dependence follows from the fast-wave dispersion, Eq.12. Increasing m within a family decreases $k_{\perp,c}^{\text{fast}}$ and increases $k_{\|}$. Equation 13 is only valid within a family; when the annulus resonance conditions transitions from one family to the next; there is a discontinuity in $k_{\perp,c}^{\text{fast}}$, which explains the piecewise linear behavior seen in Fig. 3.c.

IV. THE ROLE OF ANNULUS RESONANCES IN WAVE FIELD RECONSTRUCTIONS

In this section, we evaluate the role that AR modes play in wave-field reconstructions. While the AR modes have a very large unweighted loading resistance, they will not be strongly excited if their k values differ too much from the antenna spectrum, then they will not be strongly excited. The dependence of $k_{\|}$ of the AR modes for different m studied Sec. III (see Fig. 3) plays a central role: it defines the "trajectory" of the AR modes through the $k_{\|} - k_{\theta}$ plane and how closely it overlaps with the antenna spectral peak. This in turn determines how strongly the AR modes are excited in comparison with non-AR modes.

Section IV A develops the mathematics for how wave power is partitioned between different regions in the model and defines the amount of power that oscillates between the core and edge regions. Sections IV B and IV C present loading resistance calculations for an inter-strap antenna phasing of $\pi/2$ and $5\pi/6$ respectively for various annulus densities keeping the core density fixed. While quantitative results are presented, we emphasize the qualitatively behavior of the AR modes and their k-value relative to the antenna spectrum. We find instances where (i) the AR modes account for a large fraction of the total wave power, and (ii) a large fraction of the total wave power, over 50%, is "trapped" in the edge. Indeed, the two features are fairly well-correlated, as expected. We also find instances where the percentage of core loading is much larger, around 80%, and furthermore that the power in the edge can propagate into the core. These finding are a promising explanation for the edge loss of HHFW power on NSTX. However the case of $\pi/2$ phasing shows the *opposite* trend of fraction edge loading with increasing annulus density; namely, in this model, power trapping in the edge tends to decrease with increased annulus density. In the $5\pi/6$ phasing case, though, the power trapping is observed to increase initially with annulus density. This may be explained by magnetic pitch, as discussed in Sec. V.

A. The partition of wave power between core and edge

The expression for the Poynting flux Γ_z through a surface normal to the axial direction is given as a double sum over all modes:

$$\langle \Gamma_z \rangle = \sum_{m,n,m',n'} \int \int \Big\langle \tilde{E}_r(r,m,n)\tilde{H}^*_\theta(r,m',n') - \dots \\ \tilde{E}_\theta(r,m,n)\tilde{H}^*_r(r,m',n') \Big\rangle e^{i(k_\parallel - k'_\parallel)z + i(m-m')\theta} r dr d\theta.$$

In this sum, $k_\parallel$ is the axial wavelength for the (m,n) mode, and $k'_\parallel$ is for the $m',n')$ mode. The cross-terms indicate interefence between modes. When integrating over the entire azimuthal angle, when can apply orthogonality between the two asimuthal mode numbers m and m'. When integrating over the entire radial domain, we then have orthogonality of n and n'. In the case of both, then expression for axial wave power reduces to the sum of individual fluxes from each mode with no interference between modes.

When integration occurs over the entire azimuthal angle but not over the entire radial domain, the Poynting flux becomes

$$\langle S_z \rangle = 2\pi \sum_{m,n,n'} \int \Big\langle \tilde{E}_r(r,m,n)\tilde{H}^*_\theta(r,m,n') - \dots \\ \tilde{E}_\theta(r,m,n)\tilde{H}^*_r(r,m,n') \Big\rangle e^{i(k_\parallel - k'_\parallel)z} r dr.$$

For each m, these terms are categorized as either diagonal terms ($n = n'$) and cross-terms ($n \neq n'$). Diagonal terms have no z-dependence, but cross-terms do. If we integrate over the core, then the diagonal terms define a fixed amount of power that remains in the core, but the cross-terms define an oscillating power that can be added to and taken from the core and given to the edge as one varies z. Likewise, when integrating over the edge, the diagonal terms descrbe power that remains in the edge, which we refer to as "trapping" in the edge. The oscillating power must be computed numerically at each z-location of interest. A convenient and z-independent metric of the power available for oscillation is

$$P_{osc} = 2\pi \sum_{n \neq n'} \Big| \int \langle E_r(r,m,n)H^*_\theta(r,m,n') - \dots \\ E_\theta(r,m,n)H^*_r(r,m,n') \rangle \Big| \, r dr. \tag{14}$$

Note that no power oscillates between modes of different m values. Also, if there is one dominant mode for a given m, then the oscillating power will be a small fraction of the total wave power contained in these m-modes.

Annulus	Loading Resistance [Ω]				AR Loading		
Density	Total	Core (%)	Edge (%)	Oscillating	Core (%)	Edge (%)	Total (%)
0.5×10^{18}	2.31	1.02 (44%)	1.29 (56%)	0.21	14%	97%	60%
1.0×10^{18}	3.96	1.91 (48%)	2.04 (52%)	0.74	27%	94%	63%
1.5×10^{18}	3.93	2.68 (68%)	1.25 (32%)	0.85	23%	81%	42%
2.0×10^{18}	5.58	4.18 (75%)	1.41 (25%)	1.31	19%	76%	34%

TABLE I: Loading resistance by region and the contribution of AR modes in each n_a. The lefthand columns show the total loading, its partition into edge and core power, and the power that oscillates between core and edge (Eq. (14)). In the righthand columns, "total" denotes the percent contribution of the AR modes to the total loading, while"Edge" and "Core" columns denote the percent contribution to each region. For instance, 97% in the "Edge" column means that the AR edge power is 97% of the total edge power.

B. Current-drive phasing

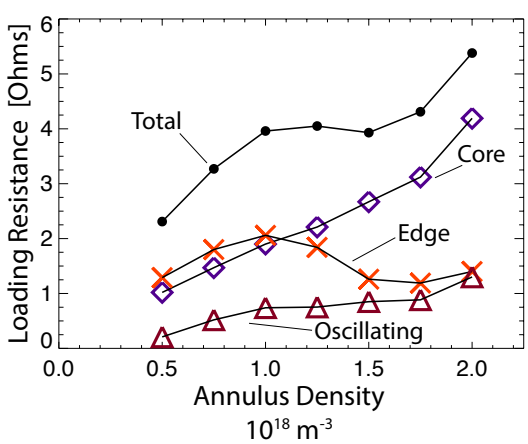

FIG. 7: Trend in loading resistance as n_a increases; circles: total loading, diamonds: core loading, plus: edge loading, triangles: oscillating power.

The results of changing the annulus density n_a in the range of 5.0×10^{17} to 2.0×10^{18} m^{-3} are summarized in Table I and shown graphically in Fig. 7. The general trend with increasing n_a over this density range is that (i) total loading increases, (ii) the fractional loading to the core increases, and (iii) the percent contribution of the AR modes decreases. The increase

in total loading with n_a results from increases in both AR and non-AR modes. The non-AR loading steadily increases with increasing n_a, which improves core loading. Meanwhile the AR loading is not monotonically increasing with n_a for reasons discussed below, and the AR contribution decreases as n_a rises. Also, the amount of power that oscillates between the edge and the core, Eq. (14), steadily increases from a small fraction ($\sim 10\%$) to nearly the full power in the edge. We might say that the power in the edge is no longer trapped there. Figure 8 plots the percent loading in the core and edge as a function of z moving away from the antenna. For $n_a = 5.0 \times 10^{17}$ m^{-3} (Fig. 8a), the oscillating power is small, and the edge power is close to its fixed value. For $n_a = 2.0 \times 10^{18}$ m^{-3} (Fig. 8b), the power in the edge is smaller, and a greater portion of it can propagate into the core. Absorption is not included in this model, but is predicted to be strong for NSTX core plasmas [25]; we expect that any wave power that penetrates the core will be absorbed there.

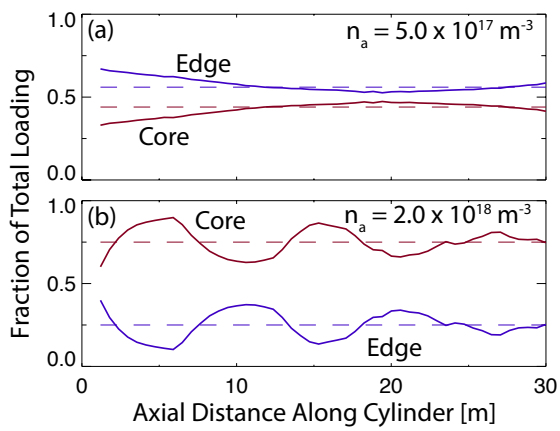

FIG. 8: Percentage of power contained in the core (red) and edge (blue) as a function of axial distance away from the antenna. Dashed lines indicated fixed percentage of power (Sec. IV A). (a) $n_a = 5.0 \times 10^{17}$ m^{-3}, and (b) $n_a = 2.0 \times 10^{18}$ m^{-3}.

A more detailed perspective is afforded by Figs. 9a and 9b. Each figure contains a contour plot of the antenna spectral power in the $k_\parallel - k_\theta$ plane. k_θ is given as m/r_a. Each contour line denoting a factor of 2 change in spectral power. Each circle denotes a mode, with lighter colors signifying a larger loading resistance. Only the largest fifty modes are plotted for clarity; these modes account for about 90% of the total wave power. The diamonds denote locations of the AR modes and show the AR trajectory through the $k_\parallel - k_\theta$ plane relative to the antenna spectrum. A diamond filled with a circle denotes an AR mode that is also

Annulus	Loading				AR contribution		
Density	Total	Core (%)	Edge (%)	Oscillating	Core (%)	Edge (%)	Total (%)
0.5×10^{18}	0.79	0.62 (79%)	0.16 (19%)	0.03	3%	97%	23%
1.0×10^{18}	1.12	0.77 (68%)	0.35 (32%)	0.07	8%	97%	36%
1.5×10^{18}	1.63	1.05 (65%)	0.58 (35%)	0.20	14%	94%	43%
2.0×10^{18}	2.16	1.46 (67%)	0.71 (33%)	0.39	18%	91%	42%

TABLE II: Effect of raising annulus density on both total loading and contribution from AR modes. Inter-strap phasing of $5\pi/6$

in the top fifty modes. At $n_a = 1.0 \times 10^{18}$ m^{-1} (Fig. 9a), the AR ridge lies directly on top of the first azimuthal sideband, with $m = 12$ being the strongest AR mode excited. This explains the relatively strong contribution of the AR modes for this density. Many non-AR modes lie on the primary antenna spectral peak. In Fig. 9b, increasing n_a to 1.75×10^{18} m^{-3} moves the AR ridge off the sideband. At the peak of the axial spectrum ($k_\parallel = 7.3$ m^{-1}), the AR ridge lies near the node in the azimuthal spectrum at $m = 8$. This explains the non-monotonic behavior in AR loading (Fig. 7. Also, for the strongest AR modes at the $m = 5$, $m = 6$, and $m = 7$, neighboring modes of the same m are also strongly excited. With several large modes of the same m, the power oscillating between core and edge increases, as explained in Sec. IV A, this oscillation is caused by interference of modes of the same m. As evidenced in Fig. 9a, typically there is only one mode strongly excited at each m in the case of $n_a = 1.0 \times 10^{18}$ m^{-3}.

For the set of AR modes, the fraction of power conducted in the edge decreases from 86% power at $n_a = 5.0 \times 10^{17}$ m^{-3} to 56% at $n_a = 2.0 \times 10^{18}$ m^{-3}. This is because higher-m AR modes conduct more power in the edge. Since the effect of increasing annulus density is to move the AR ridge to the right in $k_\parallel - k_\theta$ space, decreasing the m-value at which the AR trajectory intercepts the antenna $k_\parallel$ peak at $k_\parallel = 7.3$ m^{-1}; see Fig. 10.

C. $5\pi/6$-phasing: Heating phasing

For the NSTX antenna, $5\pi/6$ inter-strap phasing avoids a phase discontinuity between the sixth and seventh strap that would occur for $\pi/2$ phasing [26]. For $5\pi/6$ phasing, the primary

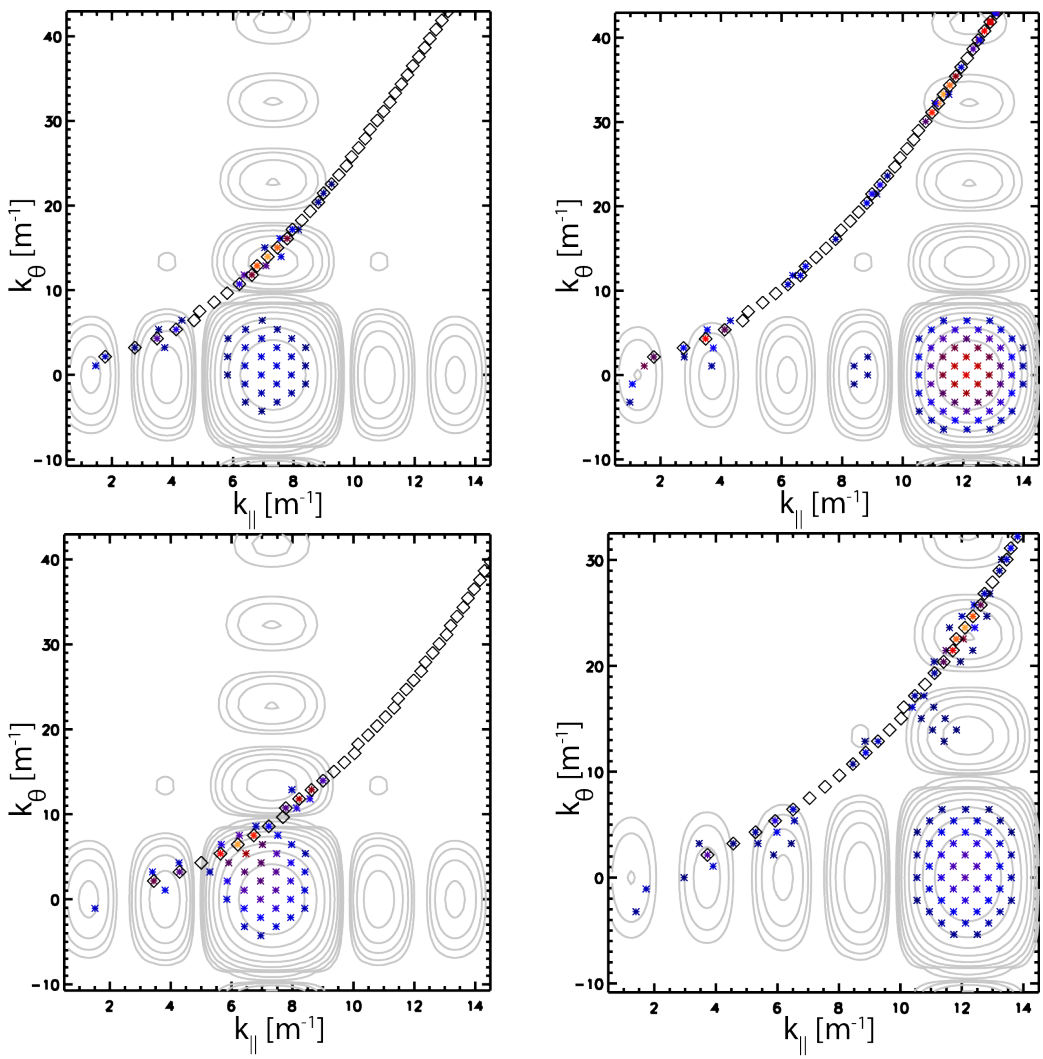

FIG. 9: Location of the AR ridge (diamonds) and largest 50 ((a) and (b)) of 100 ((c) and (d) modes (circles) relative to antenna spectral power (contour lines). (a) $pi/2$ phasing and $n_a = 1.0 \times 10^{18}$ m^{-3}, (b) $\pi/2$ phasing and $n_a = 1.75 \times 10^{18}$ m^{-3}, (c) $5\pi/6$ phasing and $n_a = 1.0 \times 10^{18}$ m^{-3}, (d) $5\pi/6$ phasing and $n_a = 2.0 \times 10^{18}$ m^{-3}.

axial spectrum peak is at $k_\parallel = 12.2$ m^{-1}. There is another second peak at $k_\parallel = -22$ m^{-1}, but the coupling to modes at such large $|k_\parallel|$ is weak enough to ignore. Table II and Fig. 11 show the loading calculations for this phasing. The total loading is reduced by roughly a factor of three compared to $\pi/2$ phasing but does steadily increase as n_a increases. Similarly, the core loading increases with n_a but at a slower rate than the $\pi/2$ case. The percentage of power in the edge is substantially smaller than with $\pi/2$ phasing but is still significant, around one third the total power. Contrary to the decrease in percent edge loading with n_a

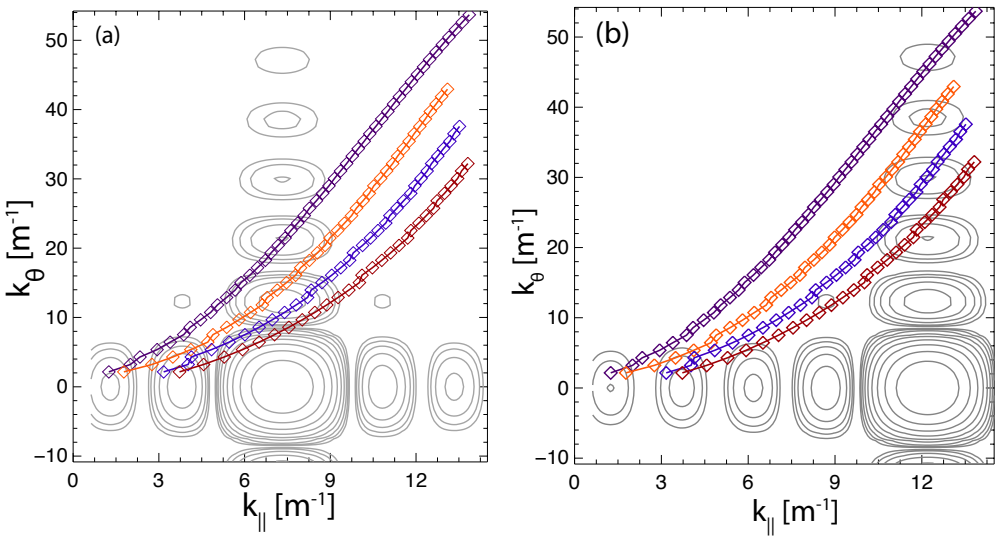

FIG. 10: Contour plot of antenna spectral power and annulus resonances (diamonds) for different n_a: from upper left to lower right, $n_a = 0.5$, 1.0, 1.5, and 2.0×10^{18} m^{-3}. (a) $\pi/2$ interstrap antenna phasing, and (b) $5\pi/6$. Increasing n_a shifts the AR ridge closer to the primary antenna spectral peaks.

seen for $\pi/2$ phasing, the percent edge loading for $5\pi/6$ phasing rises as n_a is raised from 0.5 to 1.0×10^{18} m^{-1} but level off in the range of 1.0 - 2.0×10^{18} m^{-1}. In this latter range of n_a, the power available to oscillate between edge and core increases substantially. The behavior of edge loading versus n_a is monotonically increasing, which constrasts the $\pi/2$ case and will be discussed below. The percent contribution of the AR modes is similar to the percent edge loading; for $n_a = 0.5$ and 1.0×10^{18} m^{-3}, it is substantially lower than in the $\pi/2$ case but rises instead of decreases with n_a.

Figures 9c and d show the $n_a = 1.0 \times 10^{18}$ m^{-3} and 2.0×10^{18} m^{-3} cases in the $k_\parallel - k_\theta$ plane. At $5\pi/6$ phasing, the AR trajectory now intercept the axial peak in antenna spectrum, $k_\parallel - 12.2$ m^{-1}, at substantially higher k_θ than in the $\pi/2$ case. For $n_a = 1.0 \times 10^{18}$ m^{-3} (Fig. 9c), the strongest modes are the $m = 30$, 31, and 32 AR modes, with relatively strong contribution for the $m = 38$ and 39 AR modes, whereas for $\pi/2$ phasing the strongest modes are $m = 11$, 12, and 13 AR modes. For $n_a = 2.0 \times 10^{18}$ m^{-3} (Fig. 9d), the strongest modes are the $m = 22$ and 23 AR modes, whereas for $\pi/2$ phasing the strongest modes are $m = 5$, 6, and 7 AR modes. It is only because the AR modes have such large "bare" loading resistances that they are the most strongly excited modes even when they lie on the third and fourth azimuthal sidelobes of the antenna spectrum. However, since the azimuthal

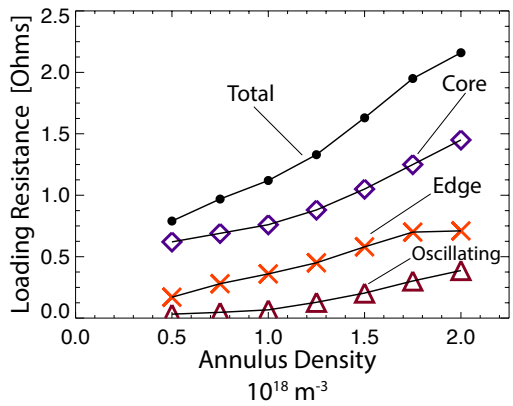

FIG. 11: Trend in loading resistance as annulus density is increased; stars: total loading, diamonds: core loading, plus: edge loading, triangles: oscillating power.

spectral weighting of the antenna scales like m^{-2} (Eq. (4)), the percent AR contribution is therefore not strong for $5\pi/6$ phasing. In fact, the wave power is more evenly distributed between modes; at $\pi/2$ phasing, 90% of the total power was carried by ~ 50 modes, whereas for $5\pi/6$ phasing it takes ~ 100 modes to reach 90%.

Finally, the "slope" of the AR ridge at $k_\parallel = 12.2$ m^{-1} is greater than at $k_\parallel = 7.3$ m^{-1}, so the AR ridge is likely to cross two adjacent azimuthal sidebands and is less likely to lie in a null between them as in Fig. 9b of the $\pi/2$ case. This explains why the edge loading increases monotonically with n_a for $5\pi/6$ phasing, in contrast to $\pi/2$ phasing. Also, for the same change in n_a, the m-value of the strongest AR modes will drop more for $5\pi/6$ phasing than for $\pi/2$ phasing.

V. DISCUSSION

The previous sections presented a conceptual framework in which the AR modes form a ridge in the $k_\parallel - k_\theta$ plane, and that increasing the annulus density, for the current model parameters, moves this ridge closer to the peak in antenna spectrum. For $\pi/2$ antenna phasing, the model predicts that the fraction of power trapped in the edge decreases as the annulus density is raised. This contradicts operational experience [6] and also results from full-wave calculations [14]. However, as the model does reproduce features of the experiments, such as over 50% of the wave power being trapped in the edge, it is important

to see if varying certain model parameters changes the AR trajectory relative to the antenna peak. Such parameters to vary include the core density and annulus width, which will be much larger for discharges with neutral beam injection.

We focus here on the potential role of field tilt of NSTX. Being a spherical torus, NSTX has a relatively weak toroidal field and a correspondingly large magnetic pitch at the outboard side, typically 30° to 40°. A preliminary approach to incorporate pitch is to rotate the projection of the mode k-vectors in the $k_z - k_\theta$ plane. Figure 12 shows how a rotation of 30° can move AR trajectory relative to the anntenna spectral peak for $5\pi/6$ phasing, and the effect is quite dramatic compared to the unrotated case of Fig. 10b. The rotated AR modes are decreased in k_θ, which would greatly increase their amplitude since the azimuthal spectral weighting scales as m^{-2}. Also, since the AR trajectory it is more horizontal (aligned with the k_z axis), we expect a broad range of AR modes to be excited by axial sidebands of the antenna spectrum. While these speculations are based on a very coarse prescription of simply rotating k, it does suggest that field pitch could have a profound impact on the model and is worth studying in a more comprehensive treatment.

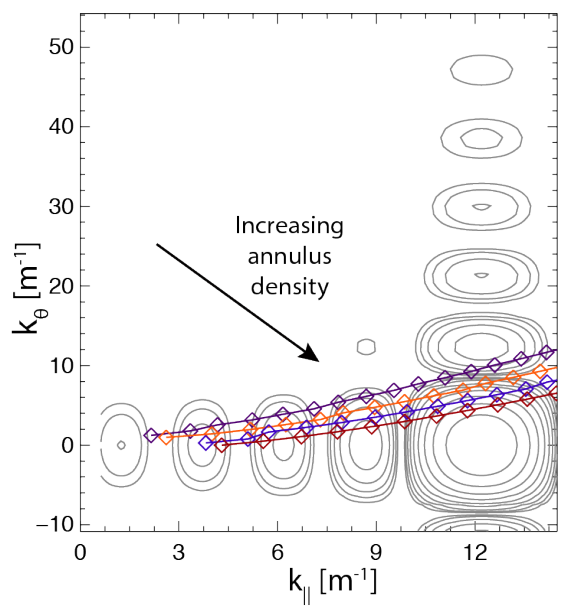

FIG. 12: Effect of a 30° rotation on the position of the annulus resonance ridge relative to the antenna spectral peaks for different densities: 0.5×10^{18} m^{-3} (purple), 1.0×10^{18} m^{-3} (orange), 1.5×10^{18} m^{-3} (blue), 2.0×10^{18} m^{-3} (red)

VI. CONCLUSIONS

In a cylindrical magnetized cold-plasma model with a two-step density profile, there exists a special class of modes that fit a half wavelength in the combined annulus-vacuum regions, have a large loading resistance, and propagate a large portion of their wave power in the edge. There is typically at most one such mode per azimuthal modenumber m, and the $k_\parallel$ value of this mode increases with m. For the model parameters selected for this paper, the underlying reason behind this relationship between $k_\parallel$ and m is because modes with the same value of $m + n$, with n the number of radial nodes, maintain the half wavelength condition over a wide range of m. Viewed in the $k_\parallel - k_\theta$ plane, these modes lie on a trajectory whose distance from the antenna spectral peaks changes with parameters such as annulus density. We have computed the relative contributions of annulus resonances and non-annulus-resonant modes as well as the fractional loading to the edge and core regions over a scan of annulus density. As expected, edge loading is large when the AR modes contribute a substantial fraction to the total loading. We note cases where over half of the *total* wave power propagates in the edge with little flux of power between the edge and core. However, while total loading always increases with annulus density, the edge loading behaves non-monotonically for the $\pi/2$-phasing case, as the AR ridge moves onto and off of azimuthal sideband of the antenna spectrum. In the case of $\pi/2$ phasing, this leads to the results that the fraction of power coupled to the core improves with edge density, in contradiction to experiments and full-wave computations. The case of $5\pi/6$ phasing shows a degradation in core loading as the annulus density increases in the range of $0.5 - 1.0 \times 10^{18}$ m^{-3} but levels off in the range $1.0 - 2.0 \times 10^{18}$ m^{-3}. Magnetic pitch could play an important role; a coarse treatment indicates that rotating the k vectors of modes by the magnetic-pitch angle at the antenna may bring the annulus resonance trajectory closer to the main spectral peak of the antenna, resulting in a large fraction of power trapped in the edge.

---

[1] Y. Ren, W. X. Wang, B. P. LeBlanc, W. Guttenfelder, S. M. Kaye, S. Ethier, E. Mazzucato, K. C. Lee, C. W. Domier, R. Bell, D. R. Smith, and H. Yuh, "Fast response of electron-scale turbulence to auxiliary heating cessation in National Spherical Torus Experiment," *Physics of Plasmas*, vol. 22, no. 11, p. 110701, 2015.

[2] E. Fredrickson, G. Taylor, N. Bertelli, D. Darrow, N. Gorelenkov, G. Kramer, D. Liu, N. Crocker, S. Kubota, and R. White, "Suppression of energetic particle driven instabilities with hhfw heating," *Nuclear Fusion*, vol. 55, no. 1, p. 013012, 2015.

[3] A. Loarte, M. L. Reinke, A. R. Polevoi, M. Hosokawa, M. Chilenski, N. Howard, A. Hubbard, J. W. Hughes, J. E. Rice, J. Walk, F. Kchl, T. Ptterich, R. Dux, and V. E. Zhogolev, "Tungsten impurity transport experiments in Alcator C-Mod to address high priority research and development for ITER," *Physics of Plasmas*, vol. 22, no. 5, p. 056117, 2015.

[4] E. Lerche, M. Goniche, P. Jacquet, D. V. Eester, V. Bobkov, L. Colas, C. Giroud, I. Monakhov, F. Casson, F. Rimini, C. Angioni, M. Baruzzo, T. Blackman, S. Brezinsek, M. Brix, A. Czarnecka, K. Cromb, C. Challis, R. Dumont, J. Eriksson, N. Fedorczak, M. Graham, J. Graves, G. Gorini, J. Hobirk, E. Joffrin, T. Johnson, Y. Kazakov, V. Kiptily, A. Krivska, M. Lennholm, P. Lomas, C. Maggi, P. Mantica, G. Mathews, M.-L. Mayoral, L. Meneses, J. Mlynar, P. Monier-Garbet, M. Nave, C. Noble, M. Nocente, I. Nunes, J. Ongena, G. Petravich, V. Petrzilka, T. Ptterich, M. Reich, M. Santala, E. Solano, A. Shaw, G. Sips, M. Stamp, M. Tardocchi, M. Tsalas, M. Valisa, and J. Contributors, "Optimization of ICRH for core impurity control in JET-ILW," *Nuclear Fusion*, vol. 56, no. 3, p. 036022, 2016.

[5] J. Hosea, R. Bell, S. Bernabei, L. Delgado-Aparicio, B. LeBlanc, C. K. Phillips, P. Ryan, S. Sabbagh, K. Tritz, J. Wilgen, J. R. Wilson, and H. Yuh, "HHFW heating efficiency on NSTX versus B_ϕ and antenna $k_\parallel$," *AIP Conference Proceedings*, vol. 933, no. 1, pp. 107–110, 2007.

[6] J. Hosea, R. E. Bell, B. P. LeBlanc, C. K. Phillips, G. Taylor, E. Valeo, J. R. Wilson, E. F. Jaeger, P. M. Ryan, J. Wilgen, H. Yuh, F. Levinton, S. Sabbagh, K. Tritz, J. Parker, P. T. Bonoli, R. Harvey, and N. Team, "High harmonic fast wave heating efficiency enhancement and current drive at longer wavelength on the National Spherical Torus Experimental," *Phys. Plasmas*, vol. 15, no. 5, p. 056104, 2008.

[7] P. M. Ryan, R. Ellis, J. C. Hosea, C. C. Kung, B. P. LeBlanc, R. I. Pinsker, G. Taylor, and J. R. Wilson, "Operating the Upgraded NSTX HHFW Antenna Array In An Environment With Li-coated Surfaces," *AIP Conference Proceedings*, vol. 1406, no. 1, pp. 101–104, 2011.

[8] J. C. Hosea, R. E. Bell, E. Feibush, R. W. Harvey, E. F. Jaeger, B. P. LeBlanc, R. Maingi, C. K. Phillips, L. Roquemore, P. M. Ryan, G. Taylor, K. Tritz, E. J. Valeo, J. Wilgen, J. R. Wilson, and the NSTX Team, "Recent fast wave coupling and heating studies on NSTX, with

possible implications for ITER," *AIP Conference Proceedings*, vol. 1187, no. 1, pp. 105–112, 2009.

[9] R. J. Perkins, J. C. Hosea, G. J. Kramer, J.-W. Ahn, R. E. Bell, A. Diallo, S. Gerhardt, T. K. Gray, D. L. Green, E. F. Jaeger, M. A. Jaworski, B. P. LeBlanc, A. McLean, R. Maingi, C. K. Phillips, L. Roquemore, P. M. Ryan, S. Sabbagh, G. Taylor, and J. R. Wilson, "High-harmonic fast-wave power flow along magnetic field lines in the scrape-off layer of NSTX," *Phys. Rev. Lett.*, vol. 109, p. 045001, Jul 2012.

[10] T. H. Stix, *Waves in plasmas*. Springer Science & Business Media, 1992.

[11] R. J. Perkins, J. C. Hosea, M. A. Jaworski, J.-W. Ahn, A. Diallo, R. E. Bell, N. Bertelli, S. Gerhardt, T. K. Gray, G. J. Kramer, B. P. LeBlanc, A. McLean, C. K. Phillips, M. Podestà, L. Roquemore, S. Sabbagh, G. Taylor, and J. R. Wilson, "The contribution of radio-frequency rectification to field-aligned losses of high-harmonic fast wave power to the divertor in the National Spherical Torus eXperiment," *Phys. Plasmas*, vol. 22, no. 4, 2015.

[12] E. F. Jaeger, L. A. Berry, E. F. D'Azevedo, R. F. Barrett, S. D. Ahern, D. W. Swain, D. B. Batchelor, R. W. Harvey, J. R. Myra, D. A. D'Ippolito, C. K. Phillips, E. Valeo, D. N. Smithe, P. T. Bonoli, J. C. Wright, and M. Choi, "Simulation of high-power electromagnetic wave heating in the ITER burning plasma," *Phys. Plasmas*, vol. 15, no. 7, 2008.

[13] D. L. Green, L. A. Berry, G. Chen, P. M. Ryan, J. M. Canik, and E. F. Jaeger, "Predicting high harmonic ion cyclotron heating efficiency in tokamak plasmas," *Phys. Rev. Lett.*, vol. 107, p. 145001, Sep 2011.

[14] N. Bertelli, E. Jaeger, J. Hosea, C. Phillips, L. Berry, S. Gerhardt, D. Green, B. LeBlanc, R. Perkins, P. Ryan, G. Taylor, E. Valeo, and J. Wilson, "Full wave simulations of fast wave heating losses in the scrape-off layer of NSTX and NSTX-U," *Nuclear Fusion*, vol. 54, no. 8, p. 083004, 2014.

[15] G. Taylor, R. E. Bell, J. C. Hosea, B. P. LeBlanc, C. K. Phillips, M. Podestà, E. J. Valeo, J. R. Wilson, J.-W. Ahn, G. Chen, D. L. Green, E. F. Jaeger, R. Maingi, P. M. Ryan, J. B. Wilgen, W. W. Heidbrink, D. Liu, P. T. Bonoli, T. Brecht, M. Choi, and R. W. Harvey, "Advances in high-harmonic fast wave physics in the National Spherical Torus Experiment," *Phys. Plasmas*, vol. 17, no. 5, p. 056114, 2010.

[16] G. Taylor, J. C. Hosea, C. E. Kessel, B. P. LeBlanc, D. Mueller, C. K. Phillips, E. J. Valeo, J. R. Wilson, P. M. Ryan, P. T. Bonoli, J. C. Wright, and R. W. Harvey, "High non-inductive

fraction H-mode discharges generated by high-harmonic fast wave heating and current drive in the National Spherical Torus Experiment," *Physics of Plasmas*, vol. 19, no. 4, p. 042501, 2012.

[17] R. J. Perkins, J. C. Hosea, N. Bertelli, G. Taylor, and J. R. Wilson, "Resonance in fast-wave amplitude in the periphery of cylindrical plasmas and application to edge losses of wave heating power in tokamaks," *Physics of Plasmas*, vol. 23, no. 7, p. 070702, 2016.

[18] B. LaBombard, R. L. Boivin, M. Greenwald, J. Hughes, B. Lipschultz, D. Mossessian, C. S. Pitcher, J. L. Terry, S. J. Zweben, and A. Group, "Particle transport in the scrape-off layer and its relationship to discharge density limit in Alcator C-Mod," *Physics of Plasmas*, vol. 8, no. 5, pp. 2107–2117, 2001.

[19] J. A. Boedo, J. R. Myra, S. Zweben, R. Maingi, R. J. Maqueda, V. A. Soukhanovskii, J. W. Ahn, J. Canik, N. Crocker, D. A. D'Ippolito, R. Bell, H. Kugel, B. Leblanc, L. A. Roquemore, D. L. Rudakov, and the NSTX Team, "Edge transport studies in the edge and scrape-off layer of the National Spherical Torus Experiment with Langmuir probes," *Phys. Plasmas*, vol. 21, no. 4, p. 042309, 2014.

[20] S. J. Zweben, R. R. Myra, W. M. Davis, D. A. D'Ippolito, T. K. Gray, S. M. Kaye, B. P. LeBlanc, R. J. Maqueda, D. A. Russell, D. P. Stotler, and the NSTX-U Team, "Blob structure and motion in the edge of NSTX," *Plasma Phys. and Controlled Fusion*, vol. 58, p. 044007, 2016.

[21] N. Bertelli, E. Jaeger, J. Hosea, C. Phillips, L. Berry, P. Bonoli, S. Gerhardt, D. Green, B. LeBlanc, R. Perkins, C. Qin, R. Pinsker, R. Prater, P. Ryan, G. Taylor, E. Valeo, J. Wilson, J. Wright, and X. Zhang, "Full wave simulations of fast wave efficiency and power losses in the scrape-off layer of tokamak plasmas in mid/high harmonic and minority heating regimes," *Nuclear Fusion*, vol. 56, no. 1, p. 016019, 2016.

[22] W. P. Allis, S. J. Buchsbaum, and A. Bers, *Waves in anisotropic plasmas*, vol. 1. The MIT Press, 1963.

[23] V. Bobkov, D. Aguiam, M. Baruzzo, D. Borodin, I. Borodkina, S. Brezinsek, I. Coffey, L. Colas, A. Czarnecka, E. Delabie, P. Dumortier, F. Durodie, R. Dux, H. Faugel, H. Fnfgelder, C. Giroud, M. Goniche, J. Hobirk, A. Herrmann, J. Jacquot, P. Jacquet, A. Kallenbach, A. Krivska, C. Klepper, E. Lerche, S. Menmuir, D. Milanesio, R. Maggiora, I. Monakhov, F. Nave, R. Neu, J.-M. Noterdaeme, R. Ochoukov, T. Ptterich, M. Reinke, A. Tuccilo, O. Tud-

isco, D. V. Eester, Y. Wang, Q. Yang, and W. Zhang, "Progress in reducing ICRF-specific impurity release in ASDEX upgrade and JET," *Nuclear Materials and Energy*, pp. –, 2016.

[24] S. Ramo, J. R. Whinnery, and T. Van Duzer, *Fields and waves in communication electronics*. John Wiley & Sons, 2008.

[25] C. Phillips, R. Bell, L. Berry, P. Bonoli, R. Harvey, J. Hosea, E. Jaeger, B. LeBlanc, P. Ryan, G. Taylor, E. Valeo, J. Wilgen, J. Wilson, J. Wright, H. Yuh, and the NSTX Team, "Spectral effects on fast wave core heating and current drive," *Nucl. Fusion*, vol. 49, no. 7, p. 075015, 2009.

[26] P. M. Ryan, D. W. Swain, J. R. Wilson, J. C. Hosea, B. P. LeBlanc, S. Bernabei, P. Bonoli, M. D. Carter, E. F. Jaeger, S. Kaye, T. K. Mau, C. K. Phillips, D. A. Rasmussen, J. B. Wilgen, and the NSTX Team, "High Harmonic Fast Wave Current Drive Experiments on NSTX," *AIP Conference Proceedings*, vol. 694, no. 1, pp. 209–212, 2003.